

Curvature Sensing-Based Pupil Alignment Method for Large-Aperture Telescopes

Qichang An¹, Hanfu Zhang¹, Xiaoxia Wu, Jianli Wang¹, Tao Chen, and Guohao Ju

Abstract—In optical systems, pupil alignment is an important component of wavefront sensing, closed-loop feedback, and imaging vignetting control because it directly affects the detection limit of the system and thus the realization of scientific goals. This study proposes the use of the energy transfer characteristics of the pupil edge to determine the misalignment of each pupil. The mechanism involves decoupling the influence of each pupil from the final exit pupil energy distribution by using aperture coding without the addition of other optical paths. The degree to which the pupil is aligned is characterized by the normalized point source sensitivity (PSSn). The pupil misalignment PSSn increased from 0.75 to 0.83. The results of this study can be used to perform tomographic detection of pupil alignment and obtain high-quality telescopic images.

Index Terms—Aperture coding, curvature sensing, large-aperture telescope, pupil misalignment.

I. INTRODUCTION

RESEARCH on important astronomical topics, such as black holes, dark matter, and the origin of the universe, requires large telescopes with an aperture size of at least 10 m [1]. The resolution and detection limit of a telescope are inversely proportional to the aperture diameter and the square of the diameter, respectively. If the diameter of an optical system is more than 10 m, the focal length can be several hundred meters; this requires precise pupil alignment along the optical path, which is difficult to achieve.

For traditional small-aperture systems, external disturbances can only produce minor rigid body displacements of the optical components. Because of the short focal length of these systems, pupil misalignment affects only adjacent pixels. Thus, improving the pupil alignment in these systems involves increasing the structural rigidity or employing image processing methods.

Manuscript received 28 December 2022; accepted 16 January 2023. Date of publication 20 January 2023; date of current version 30 January 2023. This work was supported in part by the Natural Science Foundation of China under Grants 62005279 and 61905241, in part by the Youth Innovation Promotion Association of the Chinese Academy of Sciences under Grant 2020221, and in part by Jilin Science and Technology Development Program under Grant 2022040203GH. (Corresponding author: Qichang An.)

Qichang An, Xiaoxia Wu, Jianli Wang, Tao Chen, and Guohao Ju are with the Changchun Institute of Optics, Fine Mechanics and Physics, Chinese Academy of Sciences, Changchun 130033, China, and also with the Jilin Provincial Key Laboratory of Intelligent Wavefront Sensing and Control, Changchun 130033, China (e-mail: anj@mail.ustc.edu.cn; 4601389@qq.com; wangjianli@ciomp.ac.cn; chent@ciomp.ac.cn; juguo@ciomp.ac.cn).

Hanfu Zhang is with the University of Chinese Academy of Sciences, Beijing 100039, China, and also with the Changchun Institute of Optics, Fine Mechanics and Physics, Chinese Academy of Sciences, Changchun 130033, China (e-mail: 1502597547@qq.com).

Digital Object Identifier 10.1109/JPHOT.2023.3238405

However, for large-aperture telescopes, which have long focal lengths and wide fields of view (FoVs), pupil misalignment can reduce the integrity of the edge of the FoV (i.e., cause vignetting) and limit the detection sensitivity. Off-axis stray light can further reduce the detection sensitivity. For example, in exoplanet searches, it is necessary to use a coronagraph to block the host star. If the pupil is misaligned, the starlight will leak through and diffract, reducing the contrast in the image and decreasing the likelihood of detecting an exoplanet. For wavefront sensing, pupil misalignment degrades the wavefront reconstruction accuracy and reduces the iterative correction speed, as investigated in the Thirty Meter Telescope (TMT) [10]. To address the issues stated above, this study focuses on the perception and adjustment of pupil misalignment. An example of pupil alignment performed well is the James Webb Space Telescope (JWST), which uses characteristic patterns to realize on-orbit adjustment. Specifically, a micrometric collimating telescope is used to achieve rough alignment of the optical components. The final system alignment is achieved by clipping the pupil image in front of the camera within 5% [2], [3], [4].

For long-baseline interferometric systems, pupil misalignment can also reduce the visibilities (i.e., amplitudes of the interference fringes). To overcome this, in the GRAVITY instrument of the 100-m Very Large Telescope Interferometer (VLTI), a Hartmann sensor is used to correct the pupil misalignment in three dimensions; this decreases the pupil misalignment to less than 1% [5].

The Global Astrometric Interferometer for Astrophysics (Gaia) is a space-based sky survey telescope in which the focal plane is composed of the FoVs of two telescopes. The angular accuracy of the intersection of its optical axes is 0.5 μ as. Accordingly, its pupil alignment accuracy is sufficiently high to ensure that the error caused by pupil misalignment does not affect the positioning of the optical axis. Gaia also uses a Hartmann sensor (unit size 387 μ m) for pupil surface detection, with a pupil misalignment error of less than 3% [6].

In addition, for the large-aperture collimator of the Large Optical Test and Integration Site built by Lockheed Martin in Sunnyvale, California, a method involving the bonding of a target on the mirror's surface is used to ensure the quality of the outgoing wavefront. This is done to establish a relationship between the light intensity distribution on the plane of the exit pupil and the alignment of each pupil. This is an example of the approach that aligns the pupil by measuring the energy distribution [7], [8], [9].

Adaptive optics systems in telescope are important for mitigating the impact of atmospheric turbulence and generating high-resolution images. In imaging using adaptive optics, the energy distribution between the pupil edge and the wavefront sensing element directly affects the real-time correction. This phenomenon can be observed in ultra-large-aperture telescopes owing to the utilization of a large number of optical elements to enhance pupil misalignment and a long optical path relay, which causes geometric amplification. Therefore, additional tools are needed for pupil alignment. For example, to achieve better self-adaptive correction, the Thirty Meter Telescope (TMT) uses a wavefront sensor for pupil detection to ensure that the pupil misalignment is less than 1% [10], [11], [12].

The methods stated above require an additional specific optical path for pupil alignment. Furthermore, it is impossible to simultaneously measure the system wavefront and pupil misalignment correction. The corresponding solutions based on single exit pupil measurements are prone to matrix ill-conditioning and fail to detect pupil alignment. In addition, methods based on additional wavefront sensors or reflective targets require light splitting or can only be aimed at a specific optical path [13], [14], [15], [16].

Therefore, this study proposes the use of energy transfer characteristics of the pupil edge to determine the misalignment of each pupil. Specifically, the influence of each pupil is decoupled from the final exit pupil energy distribution using aperture coding without the addition of other optical paths. Using this method, the tomographic detection of pupil alignment and high-quality telescopic imaging can be achieved.

The remaining of this paper is organized as follows. In Section II, aperture coding and curvature sensing are combined to establish the tomographic solution. In Section III, the non-out-of-plane and out-of-plane errors are analyzed and verified. We also demonstrate that this method can correct different characteristic errors. Section IV presents an experimental verification. Finally, Section V summarizes this study and draws the conclusions.

II. BASIC DERIVATION

In our analysis, a mask is introduced to coding the wavefront and the mask was mounted onto an element in the optical path of the system (or a special filter was used). If the pupil was not shifted, the energy distribution of the final focal spot was only related to the shape of the optical system. However, if the pupil was shifted, different masks produced specific energy boundary effects, which in turn affected the focal spot energy distribution. The basic principle behind pupil measurement and alignment is shown in Fig. 1, which indicates that the system wavefront and pupil alignment information can be obtained simultaneously using wavefront curvature sensing.

Wavefront curvature sensing is a technique that analyzes the wavefront based on the second derivative of the wavefront. A change in the local curvature of the wavefront causes a corresponding change in the light intensity distribution.

According to this change in the local curvature, the radial direction of the wavefront can be estimated. The difference in the light intensity along the optical axis can be used to estimate

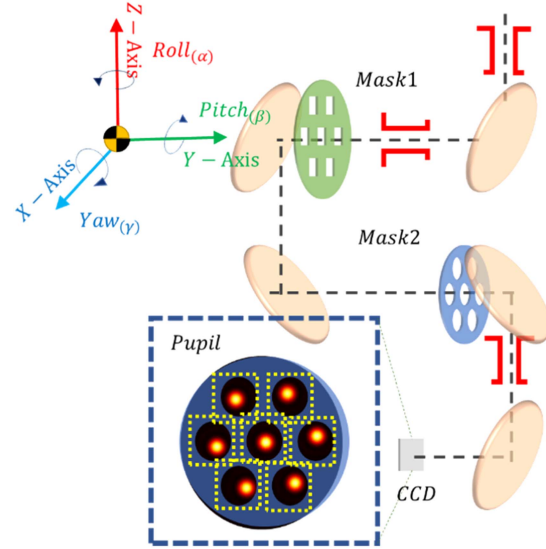


Fig. 1. Basic principle behind pupil measurement and alignment.

the wavefront curvature, and the wavefront phase information can be extracted from the curvature signal using the method that will now be described.

Suppose the system wavefront is expressed as

$$W(\mathbf{u}, 0) = \exp \left[j \frac{2\pi A}{\lambda} \sin(2\pi \mathbf{u}\mathbf{f}) \right], \quad (1)$$

where u denotes the spatial frequency and f denotes the characteristic frequency of the wavefront.

If the pre-focus light intensity distribution is

$$\begin{aligned} I_+ &= |W_+|^2 \\ &= \exp \left[\left(e^{j\pi|\mathbf{f}|^2 z_+ \lambda} - e^{-j\pi|\mathbf{f}|^2 z_+ \lambda} \right) jk (A \sin(2\pi \mathbf{u}\mathbf{f} + \varphi)) \right] \\ &= \exp \left[-2 \sin(\pi|\mathbf{f}|^2 z_+ \lambda) jk (A \sin(2\pi \mathbf{u}\mathbf{f} + \varphi)) \right], \end{aligned} \quad (2)$$

and the after-focus light intensity distribution is

$$\begin{aligned} I_- &= |W_-|^2 \\ &= \exp \left[-2 \sin(\pi|\mathbf{f}|^2 z_- \lambda) jk (A \sin(2\pi \mathbf{u}\mathbf{f} + \varphi) \right. \\ &\quad \left. + A \sin(2\pi \mathbf{u}\mathbf{f})) \right], \end{aligned} \quad (3)$$

then the curvature signal is

$$\begin{aligned} C &= \frac{I_+ - I_-}{I_+ + I_-} = \frac{-Ak\pi|\mathbf{f}|^2(\lambda z)(\sin(2\pi \mathbf{u}\mathbf{f}))}{1 - \lambda\pi k|\mathbf{f}|^2(A \sin(2\pi \mathbf{u}\mathbf{f}))} \\ &= \frac{-Ak\pi|\mathbf{f}|^2(\lambda z)(\sin(\pi \mathbf{u}\mathbf{f}))}{1 - \lambda\pi k|\mathbf{f}|^2(A \sin(2\pi \mathbf{u}\mathbf{f}))}. \end{aligned} \quad (4)$$

Next, the differential method can be used to analyze the pupil deviation. In polar coordinates, the error introduced by the small pupil position transformation can be obtained by differentiating along the axial and radial directions. The bias varies with the square of the sub-aperture position primarily because of the coupling between the rotational and positional accuracy in polar coordinates.

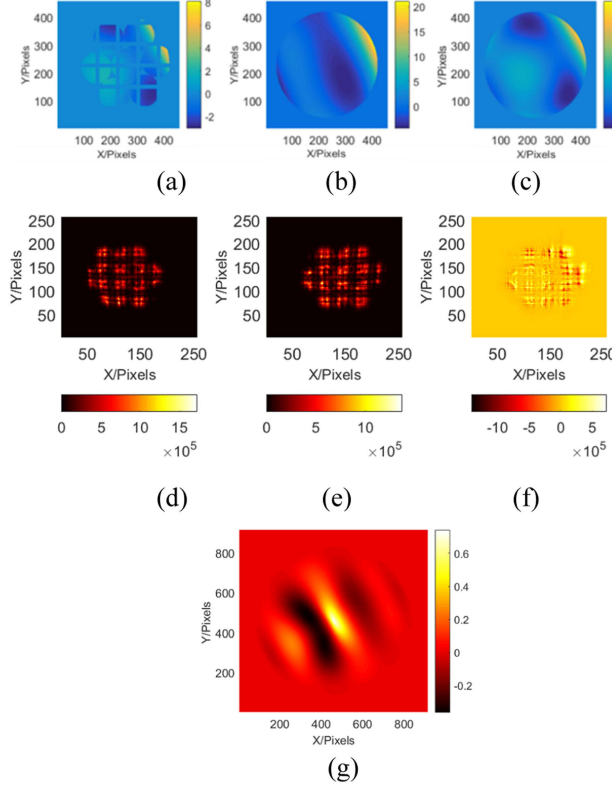


Fig. 2. Biased pupil alignment and focal spot energy distribution. (a) Wavefront after aperture coding. (b) Recovery of wavefront. (c) Original wavefront. (d) Intra-focus plane intensity distribution. (e) Extra-focus intensity distribution. (f) Intensity difference. (g) Biased pupil correlation function.

III. SIMULATION ANALYSIS

The systematic wavefront error can be divided into non-out-of-plane and out-of-plane errors. The non-out-of-plane error refers to the translation and rotational errors between the pupils, while the out-of-plane error refers to the error in the direction perpendicular to the mirror's surface. After the optical element system is coupled with the optical path, the two types of errors mentioned above can be measured.

The experiment part is mainly based on the two mirror system for verification, where we use two masks to encode the wavefront aperture, and based on this, we can verify the ability of aperture encoding to adjust the pupil maladjustment.

A. Alignment of Out-of-Plane (lateral) Error of the Pupil

A simulation of the lateral alignment of the pupil of a large-aperture telescope was conducted. The aperture coding of the superimposed aperture is presented in Figs. 2 and 3.

Owing to different misalignments in the system, the image of the defocused star displayed different energy distributions, which caused aperture deviation. By reconstructing the wavefront according to the energy distribution, the high spatial frequency variation in the wavefront caused by pupil misalignment can be determined. As can be observed from Figs. 4 and 5, the misalignment corresponding to a rectangular mask was obtained based on a circular mask.

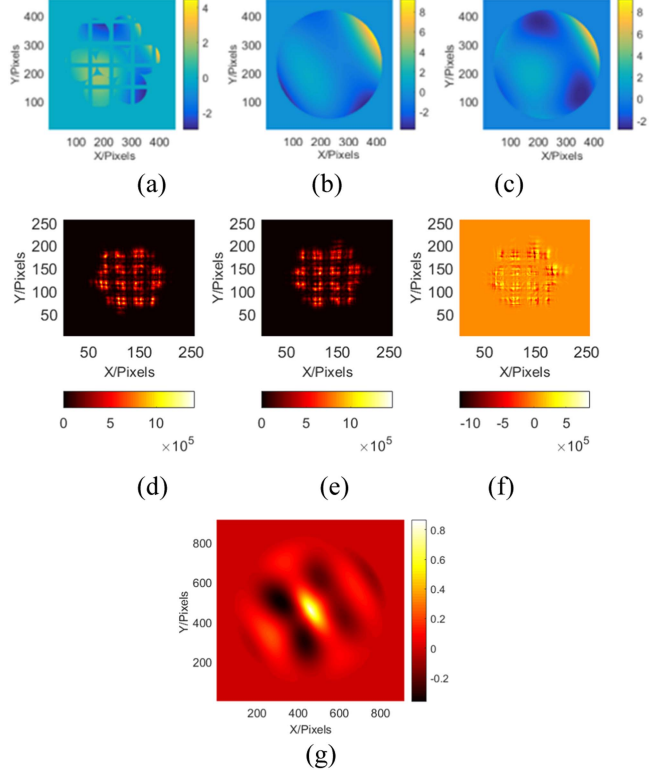


Fig. 3. Well-aligned pupil and focal spot energy distribution. (a) Wavefront after aperture coding. (b) Recovery of wavefront. (c) Original wavefront. (d) Intra-focus plane intensity distribution. (e) Extra-focus intensity distribution. (f) Intensity difference. (g) Unbiased pupil correlation function.

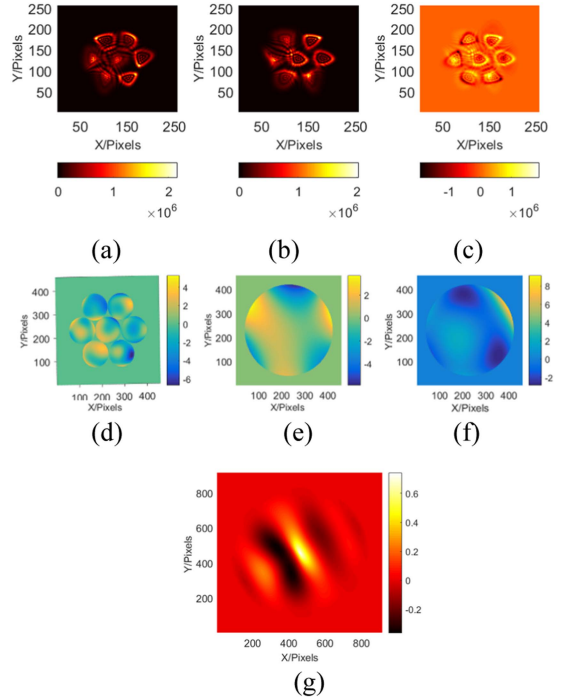


Fig. 4. Pupil longitudinal error. (a) Wavefront after aperture coding. (b) Recovery of wavefront. (c) Original wavefront. (d) Intra-focus plane intensity distribution. (e) Extra-focus intensity distribution. (f) Intensity difference. (g) Pupil correlation function.

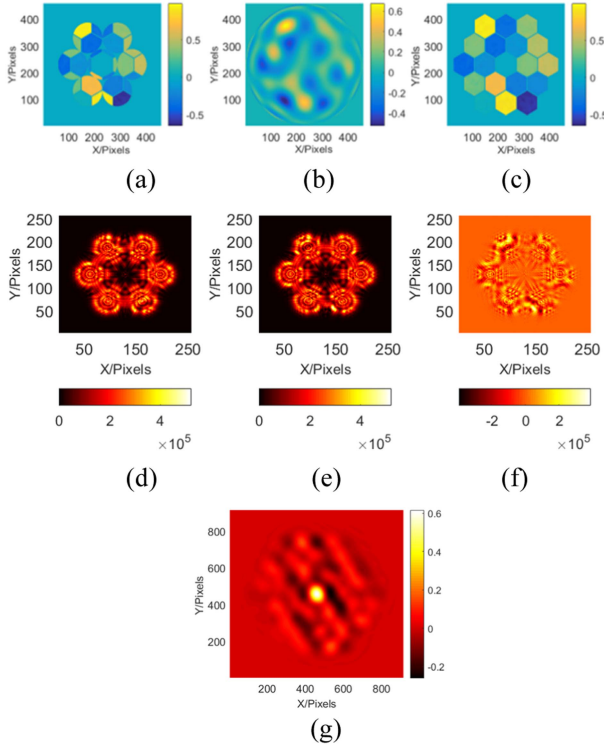


Fig. 5. Correlation distribution of the pupil longitudinal error of the segmented mirror. (a) Wavefront after aperture coding. (b) Recovery of wavefront. (c) Original wavefront. (d) Intra-focus plane intensity distribution. (e) Extra-focus intensity distribution. (f) Intensity difference. (g) Pupil correlation function.

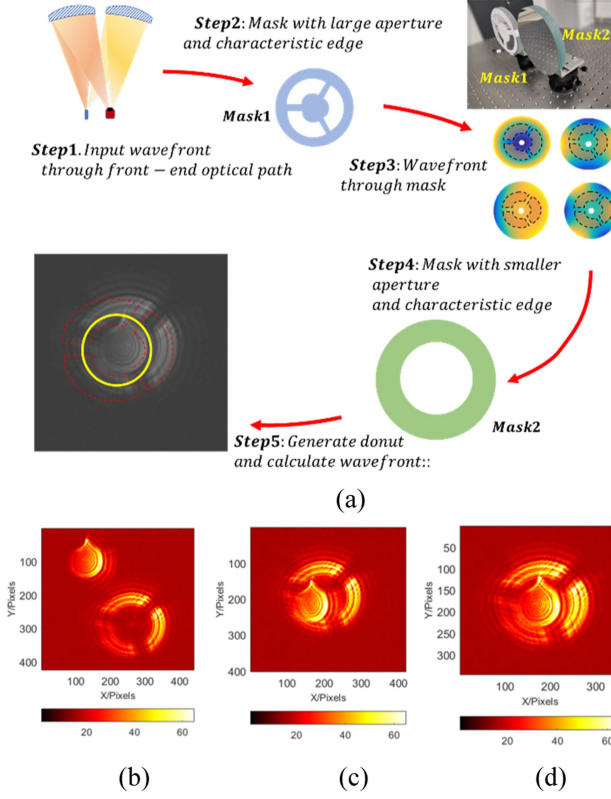


Fig. 6. Lateral alignment results and experimental setup based on curvature sensing (a) Experimental apparatus and steps (b) Initial state (c) First adjustment (d) Second adjustment.

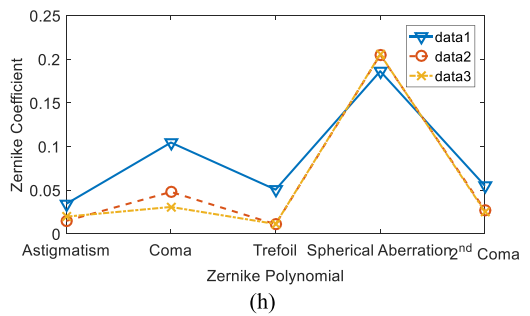
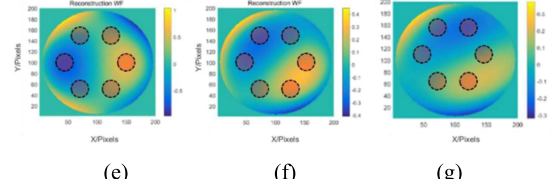
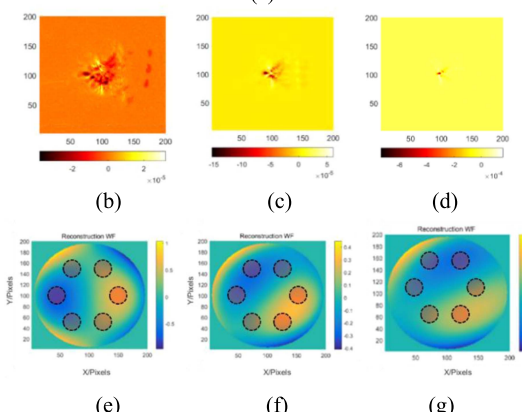
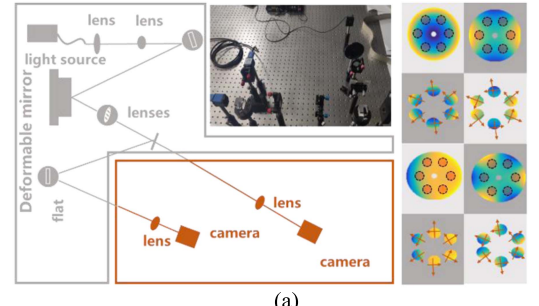


Fig. 7. Pupil longitudinal error aberration distribution and wavefront and the experimental optical path. (a) Experimental element and sub-aperture sampling position. (b)–(d) Difference in light intensity with different amplitude aberrations. (e)–(f) Wavefront reconstruction with different amplitude aberrations. (g) Comparison of each spatial frequency component. (h) Pupil longitudinal error aberration distribution and wavefront.

Traditional evaluation methods cannot directly measure pupil misalignment. Normalized point source sensitivity (PSSn) determines the average of the point spread function in the imaging area. The definition of the PSSn is

$$\begin{aligned} PSSn &= \frac{\iint_{A(x,y)} |PSF_e|^2 |PSF_{t+a}|^2}{\iint_{A(x,y)} |PSF_{t+a}|^2} \\ &= \frac{\iint_{A(fx,fy)} |OTF_e|^2 |OTF_{t+a}|^2}{\iint_{A(x,y)} |OTF_{t+a}|^2}, \end{aligned} \quad (5)$$

where PSF_e and PSF_{t+a} represent the point spread function of the telescope error and the point spread function of an ideal telescope under the influence of seeing, respectively; OTF_e and OTF_{t+a} denote the optical transfer function of the telescope

error and that of an ideal telescope under the influence of seeing, respectively; and $A(x, y)$ and $A(f_x, f_y)$ denote the integral regions of the spatial and frequency domains, respectively. According to (7), an appropriate method can be selected to calculate the PSSn. After Seo proposed the PSSn in 2009, the error distribution in the entire frequency band of the TMT has been characterized by the PSSn. In 2016, Angeli conducted a system-level modeling of the Large Synoptic Survey Telescope and analyzed the error in each frequency band using the PSSn. In 2018, Angeli used the PSSn to assign errors to the two working modes of natural seeing and surface adaptive optics of the Giant Magellan Telescope, and used a PSSn greater than one to simulate the intermediate frequency (IF) error correction link in the adaptive optics [12]. For pupil alignment, the PSSn can be multiplied by the misalignment ratio of the aperture as an evaluation index. This approach considers the optical quality of the system and the pupil alignment characteristics. For pupil alignment, the PSSn can be obtained via a correlation operation.

The PSSn is increased from 0.75 to 0.83, as shown in Figs. 2(g) and 3(g).

B. Adjustment of Out-of-Plane (longitudinal) Error of the Pupil

A longitudinal error primarily refers to defocusing. In this study, multi-dimensional sensing and fusion processing of the optical element state were performed via aperture coding and curvature sensing. The pupil longitudinal error is shown in Fig. 4; the PSSn value was 0.67.

For a segmented mirror (with 18 blocks) similar to that of the JWST, the results are presented in Fig. 5; the PSSn value was 0.61.

IV. EXPERIMENTAL VERIFICATION

A. Alignment of Non-Out-of-Plane (Lateral) Error of the Pupil

In an experiment involving pupil lateral alignment, the relative positional relationship between the two apertures was obtained using different aperture codes. In addition, using the peripheral envelope, the relative defocusing introduced by different pupils was determined. The adjustment process conducted according to the out-of-focus image of the star is presented in Fig. 6. The degree of pupil alignment was characterized by the PSSn. During our evaluation, the PSSn increased from 0.32, 0.75 to 0.89.

B. Adjustment of Non-Out-of-Plane (Longitudinal) Error of the Pupil

An anamorphic mirror was used to simulate the longitudinal wavefront error of the pupil. The experimental optical path is presented in Fig. 7(a). A lens was used to generate the basic aberration mode for comatic aberration. Data1~data3 means different measurements of different conditions, whose aberration is lower step by step(1 λ , RMS to 0.25 λ , RMS, $\lambda = 633$ nm). The PSSn values of the wavefront were 0.9633(data1), 0.9726(data2), 0.9940(data3), respectively. The difference in the focal spot distribution and the corresponding wavefront results are presented in Fig. 7(h).

Including defocusing changes and component tilts, one sub-aperture in the mask was used to sense the wavefront curvature to achieve three-dimensional correction of the pupil misalignment, which decreased the pupil misalignment to less than 5%.

V. SUMMARY AND CONCLUSION

In this study, by sensing pupil displacement and wavefront errors, high-sensitivity detection and precise astronomical observations were achieved. Through aperture coding and curvature sensing, the tomographic solution of pupil alignment was determined. Furthermore, the influence of stray light and secondary reflected light on the solution was reduced, and the detection reliability was improved.

In the future, the results of this work can effectively improve the alignment accuracy of large telescopes through targeted sensing and adjustment.

ACKNOWLEDGMENT

Thanks Dr. Hu and Dr. Wang for the help in testing. We would like to thank Editage (www.editage.cn) for English language editing.

Disclosures: The authors declare no conflicts of interest.

REFERENCES

- [1] B. T. Gansicke et al., “Accretion of a giant planet onto a white dwarf star,” *Nature*, vol. 576, no. 7785, pp. 61–64, 2019.
- [2] B. J. Bos, R. G. Ohl, and D. A. Kubalak, “Pupil alignment considerations for large deployable space telescopes,” *Int. Soc. Opt. Photon.*, vol. 8131, 2011, Art. no. 81310J.
- [3] J. G. Hagopian et al., “Optical alignment and test of the James Webb space telescope integrated science instrument module,” in *Proc. IEEE Aerosp. Conf.*, 2007, pp. 1–13.
- [4] L. G. Burriesci, J. B. Heaney, and L. G. Burriesci, “NIRCam instrument overview,” *Opt. Photon. Int. Soc. Opt. Photon.*, vol. 5904, 2005, Art. no. 590403.
- [5] J. K. Rajagopal et al., “The fiber coupler and beam stabilization system of the GRAVITY interferometer,” in *Proc. SPIE 9146, Opt. Infrared Interferometry IV*, 2014, Art. no. 914623.
- [6] J. M. Oschmann et al., “Gaia on-board metrology: Basic angle and best focus,” *Int. Soc. Opt. Photon.*, vol. 14, 2014, Art. no. 4146.
- [7] M. Coughlin et al., “A collimated beam projector for precise LSST throughput calibration,” in *Proc. SPIE 9910, Observatory Operations: Strategies, Processes, Syst. VI*, 2016, Art. no. 99100V.
- [8] D. L. Burke et al., “Calibration of the LSST instrumental and atmospheric photometric passbands,” *Int. Soc. Opt. Photon.*, vol. 14162, pp. 1–22, 2010.
- [9] M. W. Coughlin et al., “Testing of the LSST’s photometric calibration strategy at the CTIO 0.9 meter telescope,” *Proc. SPIE*, vol. 10704, pp. 753–765, 2018.
- [10] R. M. Bell et al., “LOTIS at completion of collimator integration,” *Proc. SPIE*, vol. 7017, pp. 123–135, 2008.
- [11] S. C. West et al., “Wavefront control of the large optics test and integration site (LOTIS) 65m collimator,” *Appl. Opt.*, vol. 49, no. 18, 2010, Art. no. 3522.
- [12] C. Nissly et al., “High-resolution optical modeling of the thirty meter telescope for systematic performance trades,” in *Proc. Soc. Photo-Opt. Instrum. Engineers Conf. Ser.*, 2008, Art. no. 70170U.
- [13] G. Zongchao, T. Zhen, and J. Xiangqian, “Review of geometric error measurement and compensation techniques of ultra-precision machine tools,” *Light: Adv. Manuf.*, vol. 2, 2021, Art. no. 14.
- [14] N. Roddier and F. Roddier, “Curvature sensing and compensation: A computer simulation,” *Proc. SPIE*, vol. 1114, pp. 92–96, 1989.
- [15] S. Rong and L. Richard, “Physics-based virtual coherence scanning interferometer for surface measurement,” *Light: Adv. Manuf.*, vol. 2, 2021, Art. no. 9.
- [16] Q. An et al., “Large survey camera collimation and alignment at the observation site by curvature sensing,” *Optik*, vol. 242, no. 3, 2021, Art. no. 167273.